

Robust Controller Design for an Electrostatic Micromechanical Actuator

Lili Dong^{1,*}, Jason Edwards²

¹Department of Electrical and Computer Engineering, Cleveland State University, Cleveland, OH 44115, USA

²Nasa Glenn Research Center, Cleveland, OH 44135, USA

Abstract In this paper, a robust feedback controller is developed on an electrostatic micro mechanical actuator to extend the travel range of it beyond pull-in limit. The actuator system is linearized at multiple operating points, and the controller is constructed based on the linearized model. Two kinds of controller designs are developed for set-point tracking of the actuator despite the presences of sensor noise and external disturbance. One of them is a regular fourth order Active Disturbance Rejection Controller (ADRC) and is able to achieve 97% of the maximum travel range. And the other one is a novel multi-loop controller with a second order ADRC in an inner loop and a PI controller in an outer loop. The multi-loop controller can achieve 99% of the maximum travel range. Transfer function representations of both controller designs are developed. The controllers are successfully applied and simulated on a parallel-plate electrostatic actuator model. The simulation results and frequency domain analyses verified the effectiveness of the controllers in extending the travel range of the actuator, in disturbance rejection, and in noise attenuation.

Keywords Electrostatic Micromechanical Actuator, Active Disturbance Rejection Controller, Sensor Noise, Set-point tracking, Pull-in limit

1. Introduction

Electrostatic actuation of micro-electro-mechanical systems (MEMS) makes use of the attractive electrostatic force between two charged capacitor plates to perform physical movements. With the advancement of MEMS technology, electrostatic (or micro-mechanical) actuators have been broadly used in micro-resonators, switches, micro-mirrors, accelerometers, and so on[1]. They are simple in structure, flexible in operation, and can be batch fabricated from standard semi-conductor materials such as silicon and poly-silicon[2].

The simplest electrostatic actuator has one degree of freedom and consists of one movable and one fixed capacitor plates in an electric field. When the movable plate is displaced from its original position, the capacitance formed between the two plates is changed. Therefore, one can change the displacement of the movable plate through a voltage control of the gap between both plates. However, as the gap is decreased to two thirds of the original gap, a pull-in (or snap-down) phenomenon will cause the instability of the system. As a result, the movable plate is dragged to the fixed plate, immediately reducing the gap to zero[1]. Thus

extending the travelling range of the movable plate beyond the pull-in limit has been attractive to more and more researchers. In addition, the imperfections in fabrication and packaging technology introduce system uncertainties, external disturbance and noise to the actuator system. So a controller that can stabilize the actuator system and is robust against system uncertainties, disturbance, and noise is essential for improving the performance of electrostatic actuators.

Since 1980's, both open-loop and closed-loop controllers have been applied to electrostatic actuators. Open-loop controllers have the advantages of simple structure and easy implementation. Therefore the majority of MEMS actuators are driven in open-loop mode[2]. In order to overcome pull-in limit, the most straightforward open-loop solution is to design the gap so large that the actuator is stable over the desired operating range[3]. The drawback of this approach is that the maximum gap is determined by the fabrication technology and cannot be changed by the designer. Leverage bending[4] and strain stiffening[4] are another two approaches which are used to improve the dynamic behaviour of electrostatic actuators through structure design enhancements. It is shown in[4] that both approaches extend the travel distance of the actuator to about 60% of the full gap. In addition to the structural modifications for the mechanical part of MEMS actuators, alteration of the control voltages in the electrical part has been used. Introduction of complex actuating signals to the electrostatic actuator has resulted in

* Corresponding author:

L.Dong34@csuohio.edu (Lili Dong)

Published online at <http://journal.sapub.org/control>

Copyright © 2013 Scientific & Academic Publishing. All Rights Reserved

so-called “pre-shaped control”[5], for which the dynamic model of the actuator is used to construct a pre-shaped input signal to improve the performance of it. The pre-shaped driving technique can extend the travel range of an electrostatic actuator to about 80% of its full gap. However, like other open-loop solutions, the pre-shaped control method is not robust against system uncertainties and external disturbance. The lack of accurate models, compounded by special requirements on the dynamic behaviour of actuators, has opened the possibility of closed-loop applications[5].

For closed-loop control strategies, utilizing a voltage source with a capacitor in series with the electrostatic actuator has proven successful[6, 7]. The technique shows stable operations of the actuator at 30%, 60%, and 90% of its full gap. The downside to this approach is that system uncertainties can degrade the control performance. Another disadvantage of it is that a large actuation voltage is required for the voltage source. This requirement significantly limits its feasibility. In[8, 9], a linear time-invariant (LTI) proportional gain controller is developed utilizing quantitative feedback theory (QFT). In the current literature, the LTI controller reported in[8, 9] is the only closed-loop controller that is implemented on a real MEMS actuator, and is able to extend the travelling range of it to 60% of the full gap. However a large loop gain of the LTI control system results in large noise amplification. Hence the controller cannot attenuate high-frequency input noises. More recently, nonlinear controls are applied to MEMS actuators[10]. In[11, 12], two robust nonlinear controllers are constructed based on input-to-state stabilization and back-stepping state feedback design respectively. Simulation results show that the nonlinear controllers can drive the actuator to reach full-gap traversal albeit with a large actuation voltage. But the usage of the controllers in[11, 12] is offset by their mathematical complexity and their lack of noise attenuation.

In this paper, a linear, robust, closed-loop voltage control method is developed on a parallel-plate electrostatic actuator. The controller is based on an active disturbance rejection concept. The active disturbance rejection controller (ADRC) handles unknown system dynamics effectively by treating them as an unknown disturbance and cancelling them out in control law. In addition, it is robust against external disturbance and noise. A classic ADRC consists of an extended state observer (ESO), which is used to estimate internal dynamics and external disturbance, and a PD controller, which is used to drive the system output to a reference signal. It only has three tuning parameters that are controller and observer bandwidths and controller gain. The simple configuration and easy-to-tune feature make ADRC successful in multiple applications. The classic ADRC has ever been employed to MEMS gyroscopes[13], power systems[14], automobile systems[15], and web tensions regulation[16]. In this paper, we apply both classic ADRC and a novel multiple-loop ADRC to the electrostatic actuator respectively. For classic ADRC design, the

displacement of the movable plate of an actuator is assumed available. For multiple-loop ADRC design, both displacement and charge outputs of the actuator are assumed measurable. The multi-loop design employs an ADRC for the inner loop to control the charge output, along with a PI controller in the outer loop to control the displacement output. Simulation results show that the classic ADRC design can drive the movable plate of an actuator to 97% of its full gap while the multi-loop design can achieve the traversal of 99% of the full gap. The multi-loop design also shows better noise attenuation capability than the classic one. Frequency-domain analyses proved the stability and robustness of the two designs against system uncertainties, disturbance, and noise.

2. Dynamic Modeling of MEMS Actuator

An electro-mechanical model of a simple MEMS actuator with one degree of freedom is shown in Figure 1.

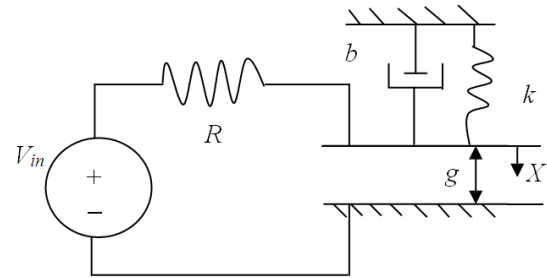


Figure 1. Micro-mechanical actuator model

In Figure1, the electrostatic actuator consists of a parallel-plate capacitor with one fixed plate and one moving plate, a spring with spring constant k , a damper with a damping coefficient b , one voltage source V_{in} and one series resistor R . The initial gap with zero applied voltage is denoted by g_0 . The gap g is positive in the direction of increasing gap, while X is the displacement of the moving plate and X is positive in the direction of decreasing gap. The relationship between g and X is given by

$$g = g_0 - X \quad (1)$$

2.1. Dynamic Modeling Using First Principles

The actuator in Figure 1 is operating in two energy domains, electrical and mechanical. As electrical charge (represented by Q) on the two plates builds up, the force of attraction grows, bringing the plates closer together. In order to keep the plates from touching each other there needs to be an equal and opposite force resisting this motion. This force is provided by the restoring spring force of a mechanical spring. In the mechanical domain, according to Newton's 2nd law, we have

$$m\ddot{X} = F_e - F_b - F_k \quad (2)$$

where $F_b = b\dot{X}$ is the linear squeeze-film damping force, $F_k = kX$ is the linear mechanical spring force and $F_e = Q^2/2\epsilon A$ is the nonlinear electrostatic force. Equation (2) can be

rewritten as

$$m\ddot{X} = \frac{Q^2}{2\epsilon A} - b\dot{X} - kX. \quad (3)$$

Note that the mass of the upper plate of the actuator is so small that the gravity force on the actuator can be disregarded.

In electrical domain, we apply Kirchhoff's circuit law to the actuator yields

$$I_{in} = \frac{1}{R}(V_{in} - V_{act}). \quad (4)$$

where V_{act} is the voltage cross the capacitor plates, and I_{in} is the current flowing through resistor R . The voltage cross actuator is

$$V_{act} = \frac{Qg}{\epsilon A}. \quad (5)$$

The current I_{in} can be solved by substituting (5) into (4). Using the fact that $I_{in} = \dot{Q}$, we have

$$\dot{Q} = \frac{1}{R}\left(V_s - \frac{Qg}{\epsilon A}\right). \quad (6)$$

Substituting (1) into (6) yields

$$\dot{Q} = \frac{1}{R}\left(V_s - \frac{Q(g_0 - X)}{\epsilon A}\right) \quad (7)$$

Equations (3) and (7) constitute the nonlinear model of the electrostatic actuator.

2.2. Equation Normalization

For the simplicity of a controller design for the electrostatic actuator, equations (3) and (7) have to be normalized. The position of the upper plate relative to the lower plate (X), time (t), the charge (Q), and the source voltage (V_{in}) are normalized as follows.

$$x = \frac{X}{g_0} \quad \tau = \omega_0 t \quad q = \frac{Q}{q_{pi}} \quad v_{in} = \frac{V_{in}}{v_{pi}} \quad (8)$$

In (8), the displacement X is normalized by the initial gap (g_0), time τ is normalized by the natural frequency (ω_0) of the actuator, charge q is normalized by the accumulation of charge at pull-in (q_{pi}), and the source voltage V_{in} is normalized by the pull-in voltage (v_{pi}). From [1] the equations that govern the pull-in voltage, the amount of charge at pull-in and the capacitance at initial gap are given by

$$q_{pi} = \frac{3}{2}C_0v_{pi}, \quad v_{pi} = \sqrt{\frac{8kg_0^2}{27C_0}}, \quad C_0 = \frac{\epsilon A}{g_0} \quad (9)$$

The details of normalization can be found in [5]. The results of the normalization are represented by

$$\ddot{x} + 2\zeta\dot{x} + x = \frac{1}{3}q^2 \quad (10)$$

$$\dot{q} + \frac{1}{r}(1-x)q = \frac{2}{3r}v_{in} \quad (11)$$

where

$$\zeta = \frac{b}{2m\omega_0}, \quad r = \omega_0 RC_0, \quad \text{and} \quad \omega_0 = \sqrt{\frac{k}{m}}. \quad (12)$$

2.3. Model Linearization

We choose the state variables of the normalized model of the actuator as $x(t)$, $q(t)$, and $s(t)$, where $s(t)$ is the velocity ($\dot{x}(t)$) of the movable plate of the actuator. For small-signal linearization, the equilibrium values of the state variables, which are represented by X_{eq} , Q_{eq} , and S_{eq} , have to be determined. Then the nonlinear equation will be linearized around these equilibrium values. The state equations of the normalized actuator model are

$$\begin{aligned} \dot{x}_1 &= x_2 = f_1 \\ \dot{x}_2 &= -x_1 - 2\zeta x_2 + \frac{1}{3}x_3^2 = f_2 \\ \dot{x}_3 &= -\frac{1}{r}(1-x_1)x_3 + \frac{2}{3r}v_{in} = f_3 \end{aligned} \quad (13)$$

The equilibrium points are determined by solving $f_1=0$, $f_2=0$, and $f_3=0$. The solutions are given by

$$S_{eq}=0, X_{eq}=(1/3)Q_{eq}^2, Q_{eq}^3-3Q_{eq}+2v_{in}=0. \quad (14)$$

From (14), we can see that when we choose different equilibrium displacement X_{eq} , we will have different Q_{eq} . The equilibrium values of X_{eq} and Q_{eq} corresponding to different percentages of the displacements with respect to full gap are calculated and given in Table 3 in Appendix. Define $X_1=X_{eq}$, and $X_3=Q_{eq}$. Then the linearized model is

$$\begin{aligned} \begin{bmatrix} \delta\dot{x}_1 \\ \delta\dot{x}_2 \\ \delta\dot{x}_3 \end{bmatrix} &= \underbrace{\begin{bmatrix} 0 & 1 & 0 \\ -1 & -2\zeta & \frac{2}{3}X_3 \\ \frac{1}{r}X_3 & 0 & \frac{1}{r}(X_1-1) \end{bmatrix}}_A \begin{bmatrix} \delta x_1 \\ \delta x_2 \\ \delta x_3 \end{bmatrix} + \underbrace{\begin{bmatrix} 0 \\ 0 \\ \frac{2}{3r} \end{bmatrix}}_B \delta V_{in} \\ \delta y &= \underbrace{\begin{bmatrix} 1 & 0 & 0 \end{bmatrix}}_C \begin{bmatrix} \delta x_1 \\ \delta x_2 \\ \delta x_3 \end{bmatrix} \end{aligned} \quad (15)$$

According to [11], we use $\zeta=2$ and $r=0.95$ for the linearized model of the electrostatic actuator in (15).

2.4. Transfer Function Representation of Linearized Model

For the convenience of later frequency-domain analyses, a transfer function representation of the linearized electrostatic actuator model is developed. Conducting Laplace transform on (15) (assuming zero initial conditions) for the displacement output gives

$$s^2 X(s) = -X(s) - 2\zeta s X(s) + \frac{2}{3}Q_{eq}Q(s), \quad (16)$$

where $X(s)$ is displacement output, and $Q(s)$ is the charge on the plates. Equation (16) can be reduced to

$$X(s) = \frac{2Q_{eq}}{3(s^2 + 2\zeta s + 1)}Q(s). \quad (17)$$

The Laplace transform of (15) for charge output is

$$rsQ(s) = Q_{eq}X(s) - (1-X_{eq})Q(s) + \frac{2}{3}V_{in}(s). \quad (18)$$

Equation (18) can be rewritten as

$$Q(s) = \frac{Q_{eq}}{(rs + (1 - X_{eq}))} X(s) + \frac{2}{3(rs + (1 - X_{eq}))} V_{in}(s). \quad (19)$$

Equations (17) and (19) can be represented by the block diagram shown in Figure 2.

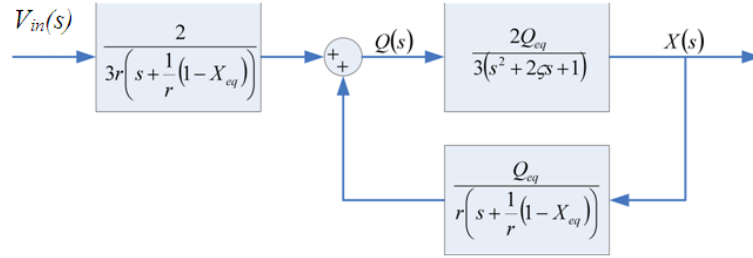


Figure 2. Transfer function model of a MEMS actuator

The block diagram shown in Figure 2 can be simplified as the one in Figure 3. From Figure 3, we can find the transfer function between displacement output and input voltage as follows.

$$\frac{X(s)}{V_{in}(s)} = \frac{4Q_{eq}}{9(rs^3 + (1 - X_{eq} + 2zeta r)s^2 + (2zeta(1 - X_{eq}) + r)s + (1 - 3X_{eq}))} \quad (20)$$

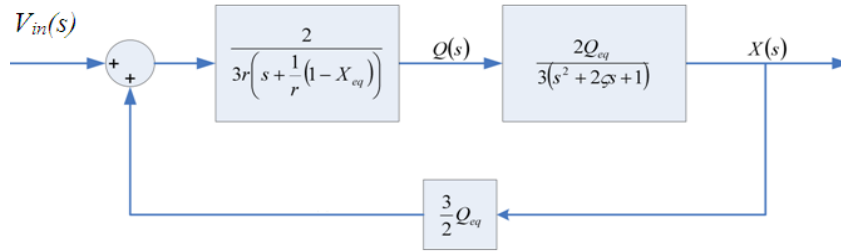


Figure 3. Simplified transfer function model

From (20), we can see that when $X_{eq} = 1/3$, the transfer function will have a pole at the origin. Any operating point with a displacement greater than $1/3$ will produce a pole in the right half plane of a complex plane. This shows explicitly how the actuator system becomes unstable at the pull-in displacement of $1/3$.

Since the transfer function representation of the actuator model (20) is a third-order plant, it can be rewritten as

$$P_{\%}(s) = \frac{b_0}{(s + a_0)(s + a_1)(s + a_2)} \quad (21)$$

where $-a_0$, $-a_1$, and $-a_2$ are poles, and the subscript % in $P_{\%}(s)$ represents the percentage of the displacement with respect to full gap. The values of parameters b_0 , a_0 , a_1 , and a_2 can be obtained by comparing (21) and (20) with the equilibrium values of X_{eq} and Q_{eq} listed in Table 3 in Appendix. The obtained parameters b_0 , a_0 , a_1 , and a_2 are given in Table 4 in Appendix.

3. Controller Design

In this section, two kinds of linear ADRC designs are presented. They are classic ADCRC and an original multi-loop ADRCs. The state space representations of the classic ADRC design are developed. Then the transfer function representations for both of the ADRC designs are derived for later frequency-domain analyses.

3.1. Classic ADRC Design

For classic ADRC, all of the system parameters in (21) are assumed to be unknown. A fourth-order extended state observer (ESO) is developed to estimate both internal system states (including displacement, velocity, and charge) and external disturbance. Based on the accurate estimation of ESO, the classic ADRC is constructed to drive the actuator's output to a desired displacement.

3.1.1. Introduction to Classic ADRC Design

From (20) and (21), the electrostatic actuator can be modeled by a third-order differential equation as follows.

$$\ddot{y} = f(y, \dot{y}, \ddot{y}, d, t) + bu \quad (22)$$

In (22), the function $f(y, \dot{y}, \ddot{y}, d, t)$, which will be denoted as f in the rest part of the paper, represents all of the other forces on the actuator plant excluding control effort, $y(t)$ is equal to normalized displacement output $x(t)$, d denotes external disturbance force, b is controller gain, and u is equal to V_{in} in (20). As we design the ADRC, the function f is assumed to be unknown and referred to as a generalized disturbance. We choose state variables as $x_1 = y$, $x_2 = \dot{y}$, $x_3 = \ddot{y}$ and $x_4 = f$, among which x_4 is an augmented state. Assuming $h = \dot{f}$ and h is bounded within the interests, (22) can be represented by a state-space model as follows.

$$\begin{aligned}\dot{X} &= AX + Bu + Eh \\ y &= Cx\end{aligned}\quad (23)$$

where

$$A = \begin{bmatrix} 0 & 1 & 0 & 0 \\ 0 & 0 & 1 & 0 \\ 0 & 0 & 0 & 1 \\ 0 & 0 & 0 & 0 \end{bmatrix}, B = \begin{bmatrix} 0 \\ 0 \\ b \\ 0 \end{bmatrix}, E = \begin{bmatrix} 0 \\ 0 \\ 0 \\ 1 \end{bmatrix}, C = [1 \ 0 \ 0 \ 0], X = [x_1, x_2, x_3, x_4]^T. \quad (24)$$

The augmented state x_4 (or generalized disturbance) and the other states can be estimated using the ESO given by (25).

$$\begin{aligned}\dot{z} &= Az + Bu + L(y - \hat{y}) \\ \hat{y} &= Cz\end{aligned}\quad (25)$$

In (25), z is the estimated state vector and $z = [z_1, z_2, z_3, z_4]^T$, where z_1, z_2, z_3 , and z_4 are the estimated x_1, x_2, x_3 , and x_4 respectively. The observer gain vector L is chosen such that all the observer poles are located at $-\omega_o$, where ω_o is observer bandwidth. As the observer gains are chosen as

$$L = [L_1 \ L_2 \ L_3 \ L_4] = [4\omega_o \ 6\omega_o^2 \ 4\omega_o^3 \ \omega_o^4]^T \quad (26)$$

the characteristic equation of the ESO is $(s + \omega_o)^4$. With a well tuned observer, the estimated states z_1, z_2, z_3 , and z_4 will closely track y, \dot{y}, \ddot{y} and f . We assume that \hat{b} is an approximate b . Then the control input to the actuator is

$$u = \frac{1}{\hat{b}}(u_0 - z_4), \quad (27)$$

where u_0 denotes a control law. Suppose $z_4 \approx f$. Then substituting (27) into (22) produces

$$\ddot{y} = u_0, \quad (28)$$

which is a triple integrator plant. The plant can be controlled by a conventional PD controller, which is

$$u_0 = k_p(r - z_1) - k_{d1}z_2 - k_{d2}z_3 - z_4, \quad (29)$$

where r denotes a desired displacement output for the actuator. In (29), k_p, k_{d1} , and k_{d2} are controller gains and are chosen as

$$k_p = \omega_c^3, k_{d1} = 3\omega_c^2, k_{d2} = 3\omega_c. \quad (30)$$

The controller gains above can place all the closed-loop poles of the controller at $-\omega_c$, which is taken as controller bandwidth.

From (26) and (30), we can see that the ADRC including the ESO only has three tuning parameters, ω_c, ω_o , and b [18]. The framework of the classic ADRC is shown in Figure 4, where d is an external disturbance, n represents sensor noise, and y_m is the measured output containing noise. In this paper, we choose controller parameters for the classic ADRC as $\omega_c = 2, \omega_o = 50$, and $\hat{b} = 1.1$.

3.1.2. Transfer Function Representation of the Classic ADRC

Combing (27) and (29), we can rewrite the control input as

$$u = \frac{1}{\hat{b}}(k_p r - [k_p \ k_{d1} \ k_{d2} \ 1]z). \quad (27)$$

Define controller gain vector as $K = [K_1, K_2, K_3, K_4] = [k_p, k_{d1}, k_{d2}, 1]$. The Laplace transform of (27) is

$$U(s) = \frac{1}{\hat{b}}(k_p R(s) - KZ(s)) \quad (28)$$

Assuming zero initial conditions for $z(t)$ and its derivatives, the Laplace transform of (25) is

$$Z(s) = (sI - A + LC)^{-1}[BU(s) + LY(s)]. \quad (29)$$

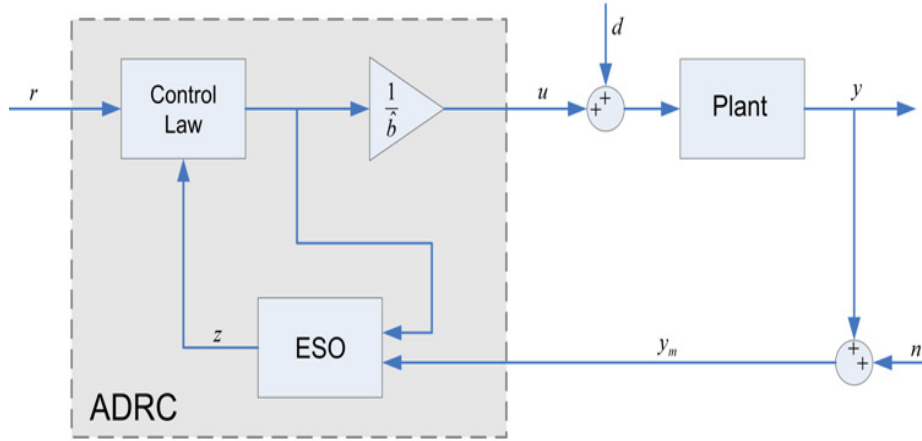


Figure 4. Framework of classic ADRC

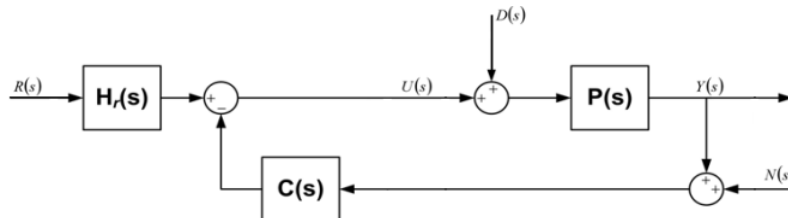


Figure 5. Block diagram of the classic ADRC control system

Substituting (29) into (28) yields

$$U(s) = \frac{1}{\hat{b}} [k_p R(s) - K(sI - A + LC)^{-1} (BU(s) + LY(s))] \quad (30)$$

Define matrix M as $M = (sI - A + LC)^{-1}$. Then (30) can be reorganized and simplified as

$$U(s) = \left[\frac{k_p}{\hat{b} + KMB} R(s) - \frac{KML}{\hat{b} + KMB} Y(s) \right] \quad (31)$$

Equation (31) can be represented by a closed-loop block diagrams shown in Figure 5, where $H_r(s)$ is a pre-filter, $C(s)$ the controller in the feedback path, $P(s)$ the actuator model, $D(s)$ an external disturbance, and $N(s)$ measurement noise.

The plant model $P(s)$, or $P_{\%}(s)$ is given by (21). The pre-filter $H_r(s)$ and controller $C(s)$ are

$$C(s) = \frac{KML}{\hat{b} + KMB} \quad H_r(s) = \frac{k_p}{\hat{b} + KMB} \quad (32)$$

Substituting the controller and observer gains into (32) yields

$$C(s) = \frac{1}{\hat{b}} \cdot \frac{c_0 s^3 + c_1 s^2 + c_2 s + c_3}{s(s^3 + d_0 s^2 + d_1 s + d_2)} \quad (33)$$

And

$$H_r(s) = \frac{1}{\hat{b}} \cdot \frac{K_1(s^4 + L_1 s^3 + L_2 s^2 + L_3 s + L_4)}{s(s^3 + d_0 s^2 + d_1 s + d_2)} \quad (34)$$

$$c_0 = K_1 L_1 + K_2 L_2 + K_3 L_3 + L_4$$

$$c_1 = K_1 L_2 + K_2 L_3 + K_3 L_4$$

$$c_2 = K_1 L_3 + K_2 L_4$$

$$c_3 = K_1 L_4$$

where

$$d_0 = K_3 + L_1$$

$$d_1 = K_2 + L_2 + K_3 L_1$$

$$d_2 = K_1 + K_2 L_1 + K_3 L_2 + L_3$$

As shown in Figure 3, the reference signal r and the measurement output y are treated independently by a pre-filter and ADRC. In addition, the configuration shown in Figure 5 allows for the derivations of traditionally defined sensitivity function (S), complementary sensitivity function (T), and other various closed loop transfer functions that are used for controller performance analyses to be conducted in the following section.

3.2. Multi-loop ADRC Design

In this section, an original multi-loop control system is developed for the electrostatic actuator. The multi-loop control system consists of a standard ADRC in an inner loop and a traditional PI controller in an outer loop. The ADRC is used to control the charge output for the electrical part of the actuator while the PI controller is employed to control the displacement output for the mechanical part of the actuator. It would be demonstrated in the next section that adding an extra measured output (charge output) to the controller design can greatly reduce the effects of sensor noise and external disturbance on the actuator system.

3.2.1. Architecture of Multi-loop Control System

We suppose the electrostatic actuator (as shown in Figure 3) can be divided into two sub-plants, which are P_1 and P_2 , along with a positive feedback constant K . The two sub-plants and the feedback constant are defined as

$$P_1 = \frac{2Q_{eq}}{3(s^2 + 4s + 1)} \quad (35)$$

$$P_2 = \frac{2/(3r)}{s + (1/r)(1 - X_{eq})} \quad (36)$$

$$K = \frac{3}{2} Q_{eq} \quad (37)$$

The output of the first sub-plant (P_1) is the displacement x . The output of the second sub-plant (P_2) is the charge q . The two sub-plants of the electrostatic actuator and the two controllers ($C_1(s)$ and $C_2(s)$) which are used to control the two sub-plants are shown in Figure 6, where $F(s)$ is a pre-filter for ADRC, and ESA denotes Electro-Static Actuator.

In Figure 6, the displacement x is controlled by a PI controller ($C_1(s)$), of which the output is u_1 . The reference signal r is the set-point for this displacement. The charge output q is controlled by an ADRC ($C_2(s)$), of which the output is u_2 . The charge output q is also acting as a control signal for the sub-plant P_1 . It is assumed both q and x are measurable. The signal u_n is the control input to the whole ESA plant. The input disturbance d in Figure 6 represents both internal and external disturbances. The block diagram in Figure 6 can be simplified as the one shown in Figure 7, where $P(s) = P_1(s)P_2(s)$.

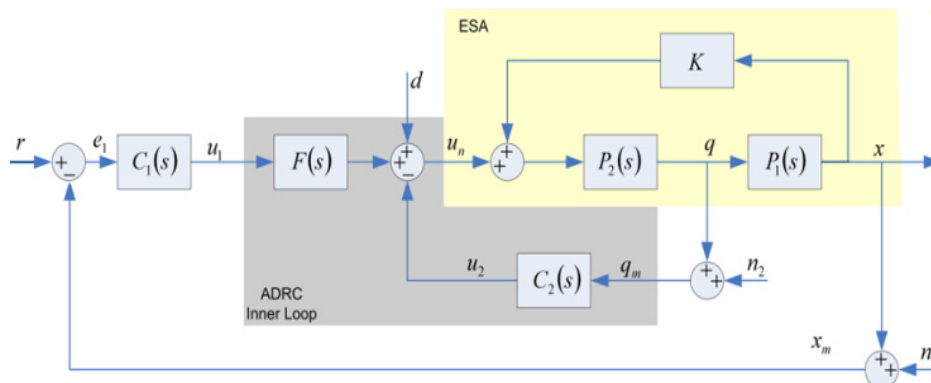


Figure 6. Multi-loop control system

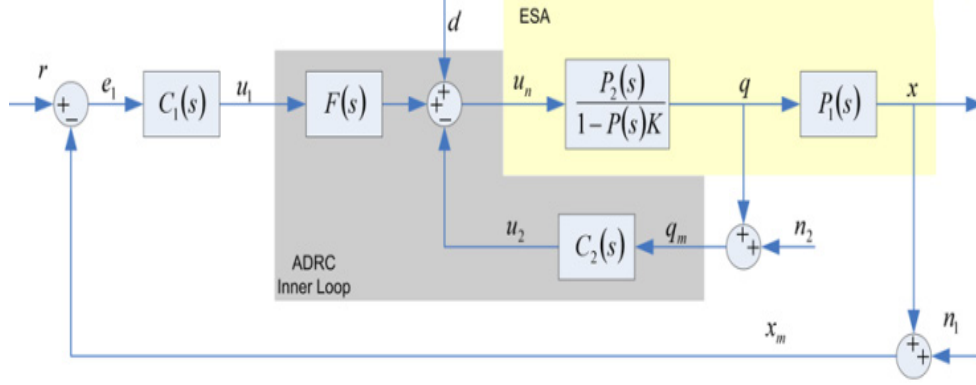


Figure 7. Equivalent model of multi-loop control system

In Figure 7, the transfer function representation of the displacement, $x(s)$ (or x), can be represented by

$$x = \frac{1}{1 + P_2 C_2 + P F C_1 - P K} (P F C_1 r + P d - P F C_1 n_1 - P C_2 n_2) \quad (38)$$

The transfer function representation of charge q is given by

$$q = \frac{1}{1 + P_2 C_2 + P F C_1 - P K} (P_2 F C_1 r + P_2 d - P_2 F C_1 n_1 - P_2 C_2 n_2) \quad (39)$$

3.2.2. Inner Loop Design

In the inner loop of the multi-loop control system (shown in Figure 6), the sub-plant $P_2(s)$ is a first-order system. Therefore an ADRC with a 2nd order ESO is applied in the inner loop. We choose the observer gain vector (L') for the 2nd order ESO as $L' = [2\omega_o, \omega_o^2]$, where ω_o is the observer bandwidth. Following the same equation development as we did for classic ADRC (in section 3.1), we will obtain the transfer function representation of the estimated charge output ($Z_1'(s)$) as

$$Z_1'(s) = \frac{2\omega_o s + \omega_o^2}{(s + \omega_o)^2} q_m(s) + \frac{s}{(s + \omega_o)^2} U_n(s) \quad (40)$$

The transfer function representation for the estimated disturbance ($Z_2'(s)$) is

$$Z_2'(s) = \frac{\omega_o^2 s}{(s + \omega_o)^2} q_m(s) - \frac{\omega_o^2}{(s + \omega_o)^2} U_n(s) \quad (41)$$

The control law used to control the inner loop is given by

$$U_n(s) = \frac{1}{b} \left[k_p' (u_1(s) - Z_1'(s)) - Z_2'(s) \right] \quad (42)$$

where the controller gain $K_p' = \omega_c$ and $\hat{b} = 2/(3\gamma)$. Substituting (40) and (41) into (42) yields

$$U_n(s) = \frac{1}{b} \left[\frac{k_p(s + \omega_o)^2}{s(s + 2\omega_o + k_p)} U_1(s) - \frac{(2\omega_o k_p + \omega_o^2)s + k_p \omega_o^2}{s(s + 2\omega_o + k_p)} q_m(s) \right] \quad (43)$$

Comparing (43) and Figure 6, we obtain the transfer function for the controller ($C_2(s)$) in the feedback path of the inner loop as follows.

$$C_2(s) = \frac{1}{b} \cdot \frac{(2\omega_o k_p + \omega_o^2)s + k_p \omega_o^2}{s(s + 2\omega_o + k_p)} \quad (44)$$

The pre-filter $F(s)$ in Figure 6 is given by

$$F(s) = \frac{1}{\hat{b}} \cdot \frac{k_p(s + \omega_o)^2}{s(s + 2\omega_o + k_p)} \quad (45)$$

The controller parameters for the ADRC are chosen as

$$\omega_c = 4 \quad \omega_o = 20 \quad \hat{b} = 0.7018 \quad (46)$$

3.2.3. Outer Loop Design

In the outer loop of multi-loop control system, a PI controller that includes a first-order noise filter is used to control the displacement output of the sub-plant $P_1(s)$ of ESA. The PI controller is defined by (47), where K_{p1} is a proportional gain, K_{d1} is an integral gain, and ω_f is the cut-off frequency of the noise filter.

$$C_1(s) = \underbrace{\frac{K_{p1}s + K_I}{s}}_{PI} \cdot \underbrace{\frac{\omega_f}{s + \omega_f}}_{Noise Filter} \quad (47)$$

The controller parameters for the PI controller are chosen as

$$K_{p1} = 2.75, K_I = 0.75, \omega_f = 100 \quad (48)$$

The two sub-controllers $C_1(s)$ (given by (47)) and $C_2(s)$ (represented by (44)) constitute the control efforts for the multi-loop control system. (4.85)

4. Stability and Robustness Analyses

In this section, we investigate the stability and the robustness against noise and disturbance for both classic ADRC and multi-loop control system designs.

4.1. Loop Transmission and Sensitivity Functions for Classic ADRC Design

In the frequency domain, the loop transmission function is a key tool in accessing the performance of a control system. For a classic ADRC design, the loop transmission function $L(s)$ in Figure 5 is defined by

$$L(s) = P(s)C(s) \quad (49)$$

From (21) and (33), we can expand $L(s)$ as

$$L(s) = P(s)C(s) = \frac{b_o}{\hat{b}_o} \cdot \frac{c_0 s^3 + c_1 s^2 + c_2 s + c_3}{s(s + a_0)(s + a_1)(s + a_2)(s^3 + d_0 s^2 + d_1 s + d_2)} \quad (50)$$

From Figure 5, the measurement output $Y(s)$ and the control signal $U(s)$ can be represented by (51) and (52). The sensitivity function $S(s)$ and complementary sensitivity function $T(s)$ are defined by (53).

$$Y(s) = \frac{H(s)P(s)}{1+P(s)C(s)}R(s) + \frac{P(s)}{1+P(s)C(s)}D(s) - \frac{P(s)C(s)}{1+P(s)C(s)}N(s) \quad (51)$$

$$U(s) = \frac{H(s)}{1+P(s)C(s)}R(s) - \frac{P(s)C(s)}{1+P(s)C(s)}D(s) - \frac{C(s)}{1+P(s)C(s)}N(s) \quad (52)$$

$$S(s) = \frac{1}{1+L(s)} \quad T(s) = \frac{L(s)}{1+L(s)} \quad (53)$$

The transfer function from the noise input $N(s)$ to the control signal $U(s)$ is denoted as $C(s)S(s)$ and is used to investigate the effects of sensor noise, and the transfer function from the disturbance input $D(s)$ to the displacement $Y(s)$ is denoted as $P(s)S(s)$ and will be used to discuss the disturbance rejection capability. The $C(s)S(s)$ and $P(s)S(s)$ are

$$C(s)S(s) = \frac{C(s)}{1+L(s)} \quad (54)$$

$$P(s)S(s) = \frac{P(s)}{1+L(s)} \quad (55)$$

4.2. Loop Transmission and Sensitivity Functions for Multi-loop Design

From Figure 7, the effects of sensor noise on the control input (u_n) to the plant are represented by

$$u_n = -\frac{FC_1(1-PK)}{1+P_2C_2+PFC_1-PK}n_1 - \frac{C_2(1-PK)}{1+P_2C_2+PFC_1-PK}n_2 \quad (56)$$

From (38), the loop transmission function ($L_1(s)$) for the primary loop (outer loop) is given by

$$L_1 = \frac{PC_1F}{1+P_2(C_2-KP_1)} \quad (57)$$

The sensitivity function for the outer loop is given by

$$S_1 = \frac{1}{1+L_1} \quad (58)$$

Substituting (57) into (59), we will have the sensitivity function rewritten as

$$S_1 = \frac{1+P_2C_2-PK}{1+P_2C_2+PC_1F-PK} \quad (59)$$

From (38), the input disturbance transfer function ($P(s)S(s)$) between input disturbance (d) and displacement output (x) is

$$P(s)S(s) = \frac{P}{1+P_2C_2+PFC_1-PK} \quad (60)$$

4.3. Stability Analyses

The Bode diagrams of the loop transmission function $L(j\omega)$ ((50)) for classic design are shown in Figure 8, where $L05$ represents the $L(j\omega)$ for the desired travel range being 5% of the full gap. The plant for this travel range is denoted by $P05$. Similarly, $L20$, $L33$, $L50$, $L75$, and $L95$ represent the loop transmission functions for the desired travel ranges being 20%, 33%, 50%, 75% and 95% of the full gap. Note that the plant $P33$ is linearized at the pull-in displacement. In Figure 8, three of the plants have unstable poles in the RHP ($P50$, $P75$, and $P95$), one has a pole at the origin ($P33$), and the other two are stable ($P05$, $P20$). The stability margins for the first design are listed in Table 1. The Bode diagrams of the loop transmission function ((57)) with respect to different displacements for multi-loop design are illustrated in Figure 9. Table 2 shows the stability margins for the multi-loop design. The bandwidth for multi-loop design is reduced but not significantly compared to classic ADRC design. Both classic ADRC and multi-loop designs have sufficiently large, positive stability margins which demonstrate the stability of these two designs.

Table 1. Stability margins for classic ADRC design

Plant Model	Gain Margin (dB)	Phase Margin (degrees)	Band Width (rad/sec)
P05	27.9	61.7	2.96
P20	21.9	77.8	6.80
P33	19.6	77.6	9.08
P50	17.8	75.3	11.3
P75	16.0	71.7	14.0
P95	15.0	69.1	15.9

Table 2. Stability margins for multi-loop design

Plant Model	Gain Margin (dB)	Phase Margin (degrees)	Band Width (rad/sec)
P05	22.2	56.6	1.92
P20	16.1	80.7	5.22
P33	13.9	79.6	7.30
P50	12.1	73.5	9.32
P75	10.2	65.1	11.6
P95	9.13	59.6	13.1

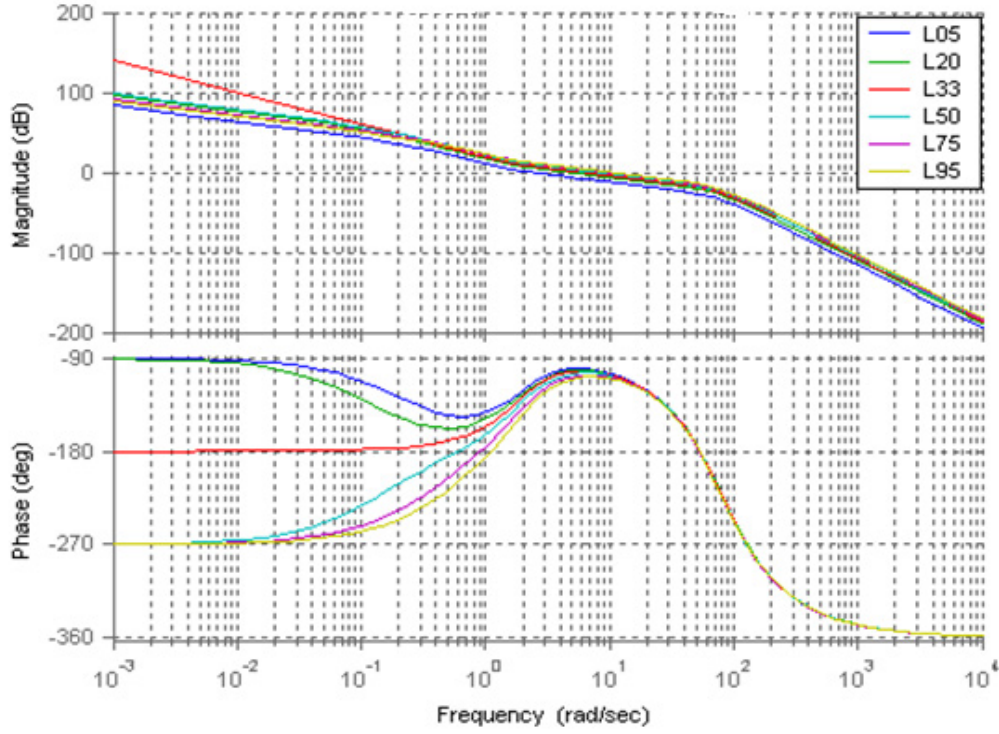


Figure 8. Bode diagrams of the transmission function for classic ADRC design

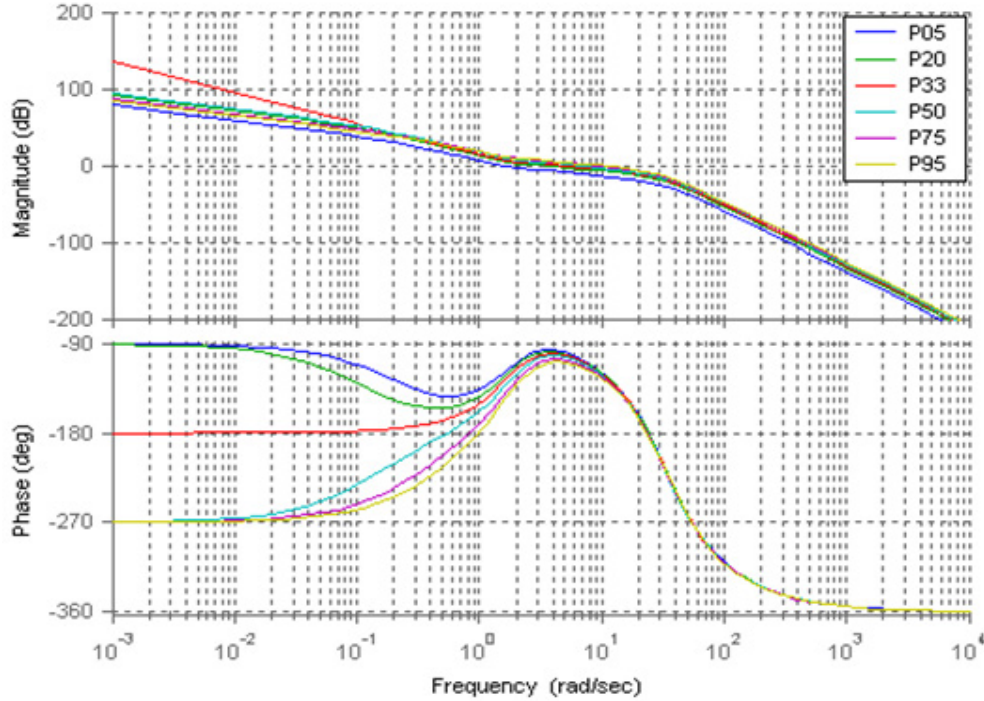


Figure 9. Bode diagrams of the loop transmission function for multi-loop design

4.4. Noise Attenuation

For multi-loop control system, the transfer functions from two sensor noise sources (n_1 and n_2) to a single controller input (u_n) are given by (56). The Bode plots of these two transfer functions (in (56)) along with the Bode plot of the noise sensitivity function (54) for classic ADRC design are

shown in Figure 10. In this figure, the multi-loop n_1 represents the Bode plot of the transfer function from noise source n_1 to control input u_n , and multi-loop n_2 represents the one from noise source n_2 to control input u_n .

From Figure 10, we can see that the multi-loop control design offers significant advantages in noise attenuation over the classic ADRC design.

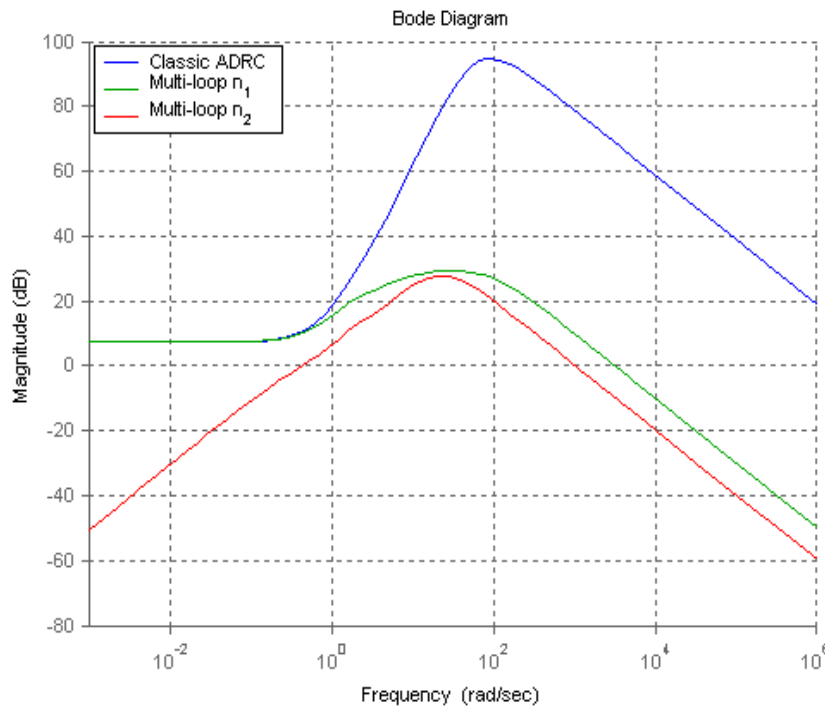


Figure 10. Magnitude Frequency Responses of Controller Noise Transfer Functions for Both Multi-loop (with noise filter) and Classic ADRC Designs

4.5. Disturbance Rejection

Figure 11 shows the Bode diagrams of the input disturbance transfer function (55), along with the transfer function of an actuator model ($P90$), the inverse of the controller (or C^{-1} from (33)) and the loop transmission function (50) for classic ADRC design. From this figure, we can see that at low frequencies, $P(s)S(s)$ (in (55)) behaves like C^{-1} , while at high frequencies, it behaves like plant model $P90$. Thus if controller C has high gain at low frequencies, C^{-1} will attenuate low frequency disturbance. It's also shown that when the magnitude of $L(s)$ is small, the controller has no control over high frequency disturbance. Then the disturbance will follow the high frequency behaviour of the actuator plant.

Figure 12 shows the bode diagrams the input disturbance transfer function (60), the transfer function of the actuator plant ($P90$), and the inverse of $F(s)C_I(s)$ in Figure 6. From this figure, we can see that the inverse of $F(s)C_I(s)$ plays a dominate role in input disturbance rejection at low frequency. However, at high frequency part, the disturbance rejection is solely dependent on the actuator plant. The electrostatic actuator has built-in disturbance rejection capabilities due to its low system gain. However, both classic ADRC design and multi-loop control system demonstrate excellent disturbance rejection capabilities at low frequency part.

In summary, the multi-loop controller is equally good as classic ADRC when it comes to stabilizing the actuator system and disturbance rejection. However, the multi-loop controller shows much better noise attenuation capability than classic ADRC design.

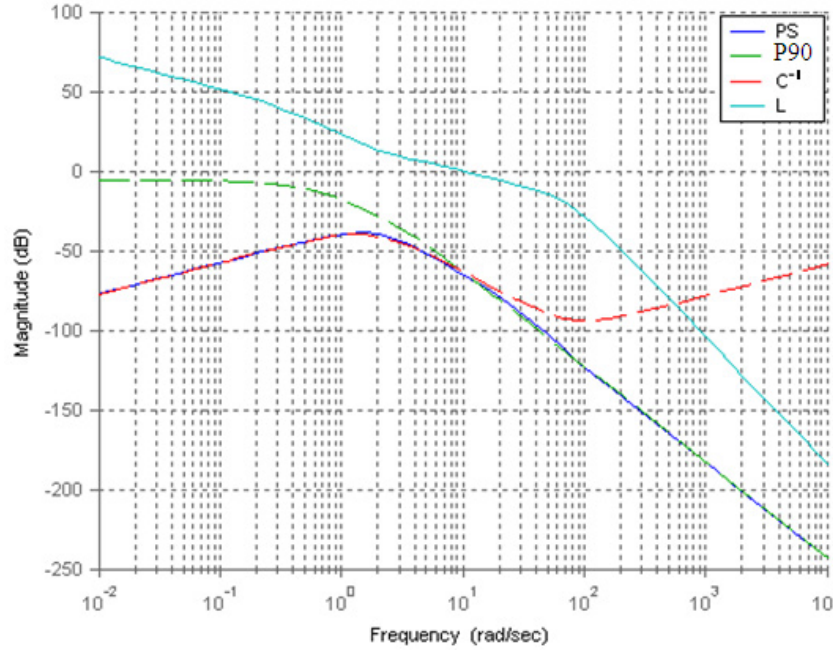


Figure 11. Bode diagrams of input disturbance function, actuator model, the inverse of controller, and loop transmission function for classic ADRC design

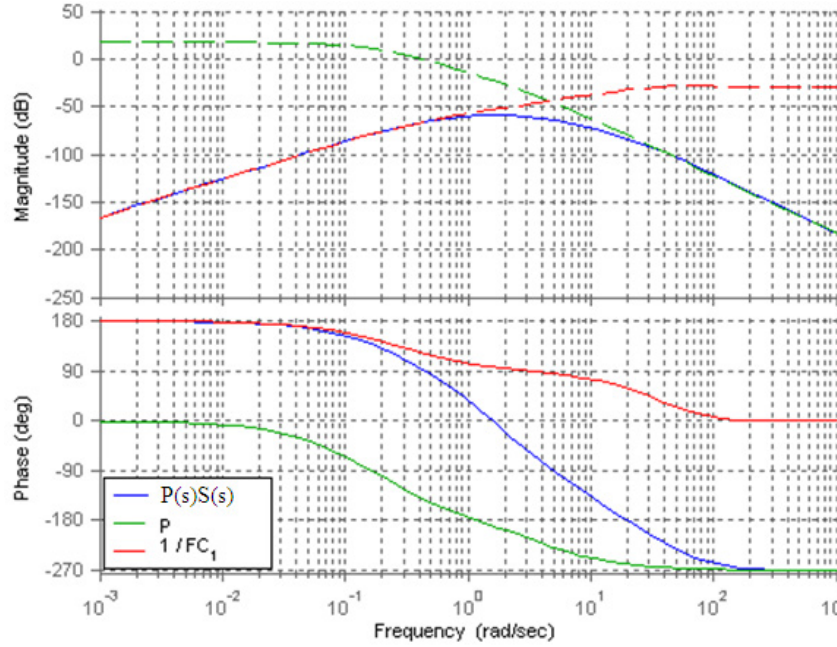


Figure 12. Bode diagrams of input disturbance transfer function, actuator model, and inverse of $F(s)C_l(s)$

5. Simulation Results

During the simulation, the sensor noise in Figure 13 is added to the control systems shown in Figure 5 (as N) and Figure 6 (as n_1 and n_2) respectively. Both the classic ADRC design and the multi-loop control system are simulated on the normalized model of the electrostatic actuator, whose parameter values are given in Table 4 of Appendix. Figure 14 and Figure 15 show the step responses of the two kinds of control designs to the references of 10% and 99% of the full gap respectively. In both figures, blue line represents reference signal. From Figure 14, we can see that the rise time of the classic ADRC is much smaller than the one for

the multi-loop controller at small displacement. However, the step response of the multi-loop control system has zero overshoot while the classic ADRC design exhibits overshoot. Figure 15 demonstrates that only the multi-loop design can achieve 99% of full gap traversal. The overshoot in the step response of the classic ADRC system will result in the “snap down” between the two plates of the actuator and cause the failure of operation. Figure 16 shows the control signals for both designs in the presence of sensor noises. It is clear to see that the multi-loop controller is a better choice in minimizing the effects of sensor noise than the classic ADRC design. Figure 17 shows the displacement outputs for the two designs with a step disturbance at $t=15s$. The figure

demonstrates the robustness of the two designs with a travel range of 97% of initial gap in the presence of the disturbance. From Figure 17, we can see that the multi-loop design has much smaller overshoot than the classic ADRC when a step disturbance is added to the system. Figure 18 compares the tracking performances of the two ADRC designs. In Figure 18, the actuator is commanded to track several desired travel ranges which are set to 10%, 30%, 50%, 70% and 90% of the full gap. Both designs have shown excellent tracking performances. The simulation results demonstrate the better performance of multi-loop control system than classic ADRC controlled system in noise attenuation and disturbance rejection. However, the classic ADRC has smaller rise time than the multi-loop design.

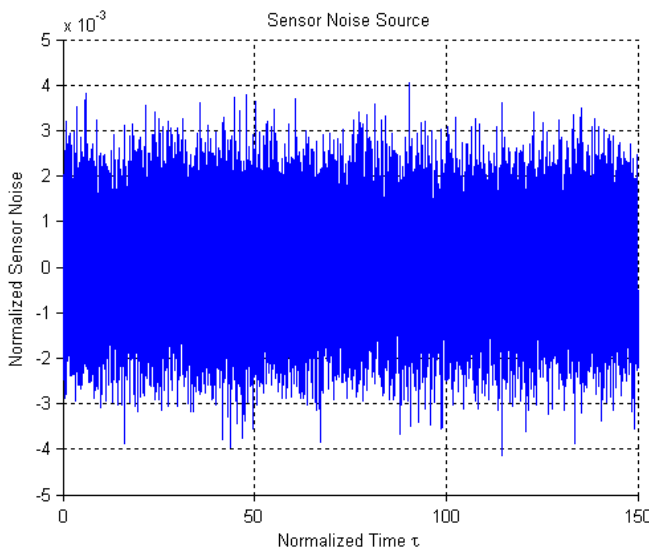


Figure 13. Normalized sensor noise

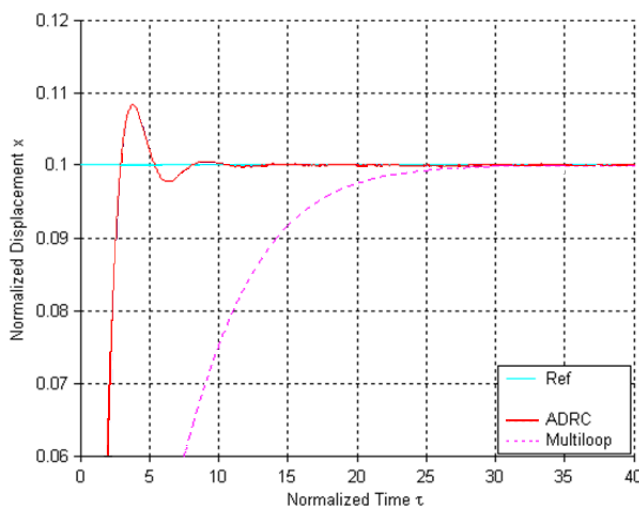


Figure 14. Step responses of two control designs at 10% of full gap

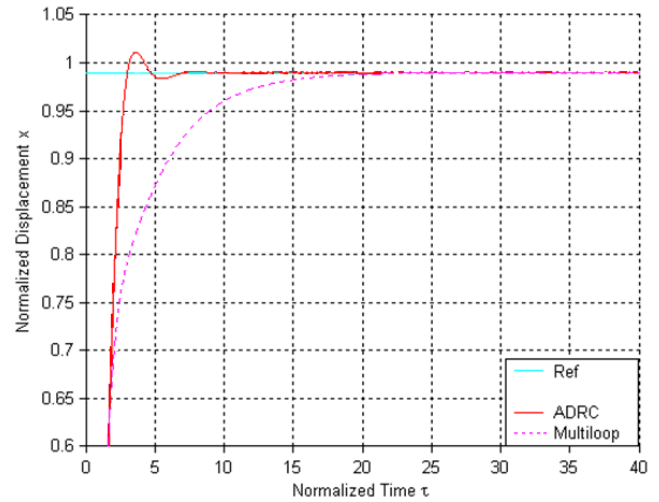


Figure 15. Step responses of two controller designs at 99% of full gap

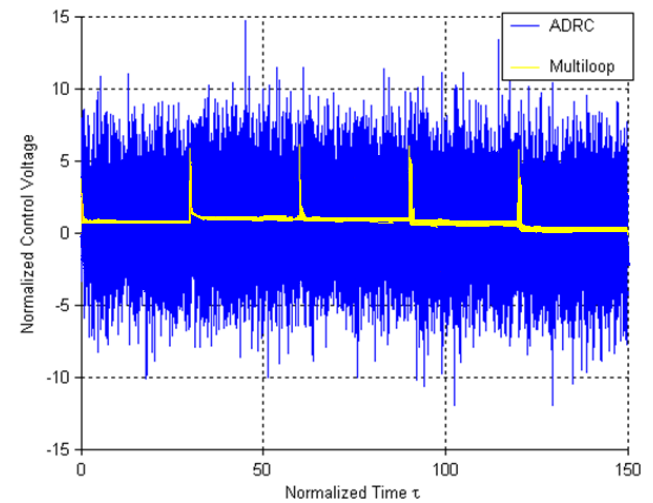


Figure 16. Controller signals for the two designs with sensor noise

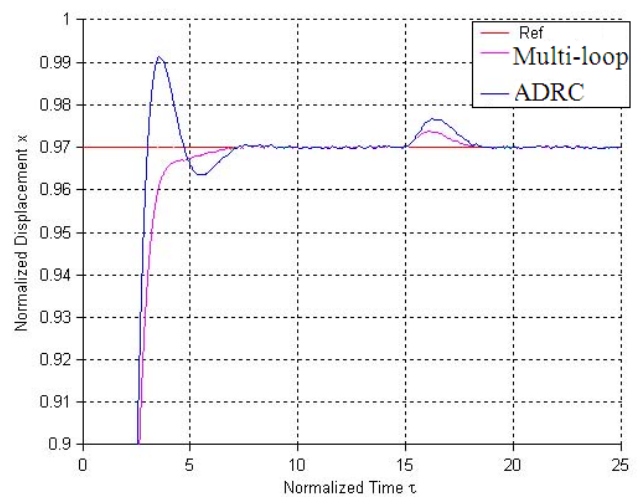


Figure 17. Displacement outputs of two designs with step input disturbances at $t=15s$

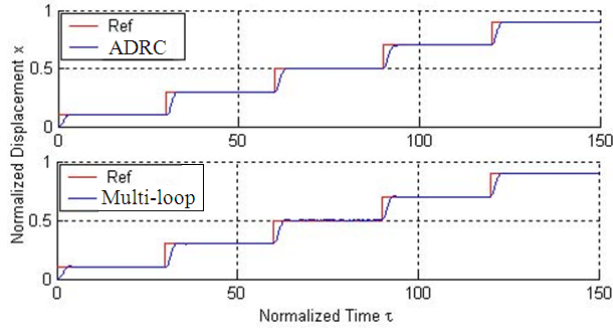


Figure 18. Displacement outputs of two designs

6. Conclusions

The research presented in the paper aims to provide a robust feedback controller that could greatly increase the operating range of an electrostatic actuator and to stabilize the actuator over the entire operating range. This controller would have to overcome the pull-in phenomenon inherent in the actuator. It also has to cope with sensor noise and external disturbance. And most importantly, the controller needs to be simple enough to implement on a MEMS device where silicon area is at a premium. The contribution of this research is that two forms of linear ADRC designs are developed that provide nearly full gap traversal for the actuator despite the presences of sensor noise and disturbances. Both controller designs have successfully addressed all the control problems state above. In addition to the effectiveness of these controllers they only have three tuning parameters, and hence are simple enough for practical implementation.

The classic ADRC design could drive the electrostatic actuator to travel 97% of its full gap. But this design is sensitive to sensor noise compared to multi-loop design. The multi-loop controller shows great promise in controlling the electrostatic actuator to 100% travel range, while keeping the effects of sensor noise to a minimum. This design should be considered as a design of the future since current technology makes it difficult to obtain two sensed outputs, but it does serve as a benchmark for what is possible with feedback control. As the complexity of MEMS devices increases, the demand for high performance control will also rise, making this design highly practical in the near future.

APPENDIX

Table 3. Equilibrium points

X_{eq}	Q_{eq}	V_{eq}
0.05	0.3873	0.5519
0.10	0.5477	0.7394
0.20	0.7746	0.9295
0.30	0.9487	0.9961
0.33	1	1
0.40	1.0954	0.9859
0.50	1.2247	0.9185

0.60	1.3416	0.8050
0.70	1.4491	0.6521
0.80	1.5492	0.4648
0.90	1.6432	0.2465
0.95	1.6882	0.1266

Table 4. Parameter values with varying displacement

Plant	b_0	a_0	a_1	a_2
P_{05}	0.18119	3.721	1.050	0.2290
P_{10}	0.25624	3.710	1.048	0.1895
P_{20}	0.36238	3.689	1.044	0.1093
P_{30}	0.44383	3.669	1.041	0.0276
P_{33}	0.46784	3.662	1.104	0.0000
P_{40}	0.51249	3.650	1.038	-0.0556
P_{50}	0.57298	3.631	1.035	-0.1400
P_{60}	0.62767	3.614	1.033	-0.2256
P_{70}	0.67796	3.597	1.031	-0.3122
P_{80}	0.72477	3.581	1.029	-0.3999
P_{90}	0.76873	3.566	1.028	-0.4883
P_{95}	0.7898	3.559	1.027	-0.5329

REFERENCES

- [1] S.D. Senturia, *Microsystem Design*, Kluwer Academic Publishers, Norwell, MA, 2001.
- [2] Kovacs G. T. A. 1998, *Micro-machined Transducers Sourcebook*, McGraw-Hill, New York.
- [3] J. Seeger, "Charge control of parallel-plate, electrostatic actuators and the tip-in instability," *Journal of Micro-electro-mechanical Systems*, vol. 12, no. 5, pp. 656-671, Oct. 2003.
- [4] E. S. Hung and S. D. Senturia, "Extending the travel range of analog-tuned electrostatic actuators," *Journal of Micro-electro-mechanical Systems*, vol. 8, no. 4, pp. 497-505, Dec. 1999.
- [5] B. Borovic, "Open-loop versus closed-loop control of MEMS devices: choices and issues," *Journal of Micromechanics and Micro-engineering*, vol. 15, no.10, pp. 1917-1924, Jul. 2005.
- [6] J. Seeger and S. Crary, "Stabilization of electro-statically actuated mechanical devices," *IEEE International Conference on Solid-State Sensors and Actuators*, pp. 1133-1136, Jun. 1997.
- [7] E. Chan and R. Dutton, "Electrostatic micromechanical actuator with extended range of travel," *Journal of Micro-electro-mechanical Systems*, vol. 9, no. 3, pp. 321-328, Sep. 2000.
- [8] S. Zhang, C. Zhu, J. K. O. Sin, and P. K. T. Mok, "A novel ultrathin elevated channel low-temperature poly-Si TFT," *IEEE Electron Device Lett.*, vol. 20, pp. 569-571, Nov. 1999.
- [9] M. Wegmuller, J. P. von der Weid, P. Oberson, and N. Gisin, "High resolution fiber distributed measurements with coherent OFDR," in *Proc. ECOC'00, 2000*, paper 11.3.4, p. 109.
- [10] G. Zhu, J. Levine, and L. Praly, "Improving the performance of an electrostatically actuated MEMS by nonlinear control:

- some advances and comparisons,” in Proc. of the 44th IEEE Conference on Decision and Control, pp. 7534-7539, Dec. 2005.
- [11] G. Zhu, J. Levine, and L. Praly, “On the differential flatness and control of electro-statically actuated MEMS,” in Proc. of 2005 American Control Conference, Portland, Oregon, pp. 2493-2498, June 2005.
- [12] G. Zhu, J. Penet, and L. Saydy, “Robust control of an electro-statically actuated MEMS in the presence of parasitics and parametric uncertainty,” in Proc. of the 2006 American Control Conference, pp. 1233-1238, Jun. 2006.
- [13] L. Dong, D. Avanesian, “Drive-mode Control for Vibrational MEMS Gyroscopes”, IEEE Transactions on Industrial Electronics, vol. 56, no. 4, pp. 956-963, Apr. 2009.
- [14] L. Dong, Q. Zheng, Z. Gao, “On Control System Design for the Conventional Mode of Operation of Vibrational Gyroscopes”, IEEE Sensors Journal, vol. 8, no. 11, pp. 1871-1878, Nov. 2008.
- [15] L. Dong, Y. Zhang, Z. Gao, “A Robust Decentralized Load Frequency Controller for Interconnected Power Systems”, *ISA Transactions*, vol. 51, no. 3, pp. 410-419, May 2012.
- [16] L. Dong, P. Kandula, Z. Gao, D. Wang, “A Novel Controller Design for Electric Power Assist Steering Systems”, *Journal of Intelligent Control and Systems*, vol. 15, no. 1, pp. 18-24, Mar. 2010.
- [17] Y. Hou, Z. Gao, F. Jiang, and B. Boulter, “Active disturbance rejection control for web tension regulation,” in Proc. of the 40th IEEE Conference on Decision and Control, vol. 5, pp. 4974-4979, Orlando, Florida, USA, Dec. 4-7, 2001.
- [18] Z. Gao, “Scaling and bandwidth-parameterization based controller tuning”, in Proc. of American Control Conference, Denver, CO, June 2003, vol. 6, pp. 4989 - 4996.